Advanced Functional Materials

ADVANCED FUNCTIONAL MATERIALS
www.afm-journal.de

RESEARCH ARTICLE

Revealing the Roles of CuF_2/NiF_2 Incorporation in the Electrochemical Performance of FeF_3 Cathodes in Solid-State Batteries

Keng Xu[1] | Kangxuan Xia[2] | Ru Xiao[1] | Ryan Grant[1] | Ruihao Deng[1] | Ruixin Wu[1] | Ratnottam Das[1] | Bowen Shao[1] | Enyuan Hu[2] | Fudong Han[1]

[1]Department of Mechanical, Aerospace and Nuclear Engineering, Rensselaer Polytechnic Institute, Troy, New York, USA | [2]Brookhaven National Laboratory, Upton, New York, USA

Correspondence: Fudong Han (hanf2@rpi.edu)

Received: 24 December 2025 | **Revised:** 5 March 2026 | **Accepted:** 12 March 2026

Keywords: conversion cathodes | cycling stability | iron fluorides | solid-state batteries | voltage hysteresis

ABSTRACT

Mixed metal fluorides have been considered as a promising candidate to lower the voltage hysteresis of conversion-type iron fluoride cathodes, but their cycling stability is limited due to transition metal dissolution and interphase growth in liquid electrolyte batteries. Here, we study the role of incorporating CuF_2 and NiF_2 in the electrochemical performance of FeF_3 cathode in halide-based solid-state batteries to test whether we can transfer the kinetic benefit of low voltage hysteresis to solid-state batteries while using solid electrolyte to eliminate transition metal dissolution and stabilize the interphase. Synchrotron X-ray absorption spectroscopy results indicated the redox reactions are attributed to Cu^0/Cu^+ and Fe^0/Fe^{2+} in $25CuF_2$-$75FeF_3$ and Ni^0/Ni^{2+} and Fe^0/Fe^{3+} in $10NiF_2$-$90FeF_3$. While no apparent improvement in electrode kinetics can be observed, the incorporation of CuF_2 and NiF_2 can largely improve the cycling stability of FeF_3 cathodes. The results demonstrate the advantages of using solid-state concept to improve the cycling stability of conversion-type cathodes.

1 | Introduction

The growing interest in electrifying transportation has led to a higher demand for the energy density of lithium-ion batteries (LIBs) [1]. As the energy density of conventional LIBs approach their physicochemical limits [2], conversion-type iron fluorides (FeF_2/FeF_3) have received renewed interest as next-generation cathodes because they can accommodate multiple electron transfers per redox center, offering 200% to 300% higher theoretical energy density than state-of-the-art intercalation cathodes, without using expensive and scarce minerals such as Co and Ni [3–12]. Despite these great promises, practical application of these cathodes has proven challenging due to large voltage hysteresis and limited cycling stability during charge/discharge cycles [11, 13–17]. Since the initial reports in early 2000s, considerable efforts have been made to understand the fundamentals of the reaction mechanisms for the development engineering approaches to address these performance challenges [13, 18–32].

The widely accepted theory of the conversion reaction mechanism is based on reconstructive phase transitions [4, 7, 8]. For FeF_2, a direct conversion from FeF_2 to LiF and Fe occurs upon lithiation [33]. In the case of FeF_3, the reaction progresses by an initial reduction via the insertion of Li ions to form $Li_xFe_yF_z$ intermediate phases and FeF_2, followed by direct conversion to LiF and Fe [8]. The reductions of both FeF_2 and FeF_3 involve

Keng Xu and Kangxuan Xia equally contributed to this paper.

significant changes both chemically and structurally. However, these understandings were challenged by recent studies on characterizing structural evolutions of FeF_2 and FeF_3 electrodes during charge/discharge. By in situ visualization of the spatial and crystallographic correlation between the parent and converted phases through TEM, Karki et al., first reported that the reaction mechanism from FeF_2 to LiF and Fe is topotactic transformation in nature, involving transport of Li^+ and Fe^{2+} within the F-anion sublattice that retained throughout the entire discharge process [22]. Subsequently, Xiao et al., demonstrated that the reduction of FeF_2 during discharge involves the formation of intermediate rutile and rocksalt Li-Fe-F phases before fully reducing to LiF and Fe, but reaffirms that the transformation of FeF_2 to rutile to rocksalt to LiF is entirely topotactic involving the intercalation and diffusion of cations in the fluorine anion sublattice [24]. A recent report from Hua et al. also provided additional evidence on the clear topological relationship of the fluorine anion sublattice between the parent and intermediate metal fluorides and LiF during the reduction of FeF_3 [25]. The fundamental knowledge of the reaction mechanisms of both FeF_2 and FeF_3 significantly deviates the conventional belief of a "conversion" reaction and highlights the important roles of intermediate phase formation, interfaces, and transition metal mobility for further development of these battery electrodes [26].

On the other hand, various engineering approaches including utilization of various nanocomposites, nanostructuring, cation and anion substitutions, electrolyte formulation, have been developed to address the performance challenges of iron fluoride cathodes [12, 15, 34–45]. Among all the approaches, incorporating another cation through doping, substitutions, or forming a composite, have received intense interest. Introducing small contents of dopants such as Ti [46], Co [20, 47], Cr [48, 49], Mn [50], Al [51], Nb [52], and Ni [53] can reportedly change the electronic structure of iron fluorides and thus improve the electronic conductivity. Despite improved rate performances, the effect of these dopants on reducing the voltage hysteresis of iron fluoride cathodes is limited. In 2015, Wang et al. demonstrated that the incorporation of 50 mol% CuF_2 in FeF_2 to form a solid solution $Cu_{0.5}Fe_{0.5}F_2$ can significantly lower the voltage hysteresis of FeF_2 from 1.6 to 0.5 V [19]. The authors attributed the enhanced kinetics to: (i) during discharge, the formation of Cu and LiF at high potential from Cu conversion helps accelerate Fe conversion because of the enhanced electronic conductivity (due to the presence of metallic Cu) and the increased ionic transport at the LiF/FeF_2 interface and (ii) during charge, the existing Fe-F framework and the high mobility of Cu ions can lower the nucleation barrier for Cu-F formation [19]. This work represents a pioneering example of improving electrode kinetics by cation substitution. The effective enhancement in reaction kinetics is also supported by a recent study from Li et al., that shows the catalytic effect of Cu-Fe dual metal nanodomains for reconversion of LiF to transition metal fluoride [54]. Despite the enhanced kinetics, a quick capacity decay can be observed for the first few cycles, due to Cu dissolution in the liquid electrolytes [19, 55], highlighting the challenges for practical application of these cathodes. Nevertheless, recent work from Gordon et al., [21]. and Huang et al., [23]. suggests that enhanced kinetics may not be achieved for all ternary iron difluorides, as no decreases in the voltage hysteresis can be observed for $Ni_xFe_{1-x}F_2$, $Co_xFe_{1-x}F_2$, and $Mn_xFe_{1-x}F_2$ solid solutions due to enhanced interphase growth from the side reactions between the ternary fluorides and liquid electrolytes [21, 23]. In addition, although it is more widely reported for Cu [55, 56], other transition metals such as Ni, Co, Mn, and Fe also have slight solubility in common liquid electrolytes [12, 57], leading to active material loss, diffusion of dissolved transition metal to the anodes and thickening of solid electrolyte interphase. Given the large effects of dissolution and interphase formation, the exact role of cation substitution in improving the electrochemical performance of iron fluoride cathodes remains elusive. It should also be noted that, despite starting from a solid solution ternary difluoride where all transition metals should have an oxidation state of +2, Fe^{3+} have often been detected after the first charge [19], suggesting the structural irreversibility of these cathodes.

One effective approach to addressing the dissolution issue is replacing liquid electrolytes with solid electrolytes to make solid-state batteries [58–65]. The utilization of solid electrolytes can also help mitigate the particle displacement as well as form a less dynamic interphase (no need to reform part of the interphase upon pulverization/cracking), improving the cycling stability of iron fluoride cathodes [66]. Moreover, integrating iron fluoride cathodes with solid electrolytes may provide additional kinetic benefits due to the absence of concentration polarization in the liquid electrolytes and the larger content of Li ion per volume of electrolyte [20]. The utilization of polymer-based solid electrolyte helps improve the cycling stability of FeF_2 cathodes at elevated temperatures (50°C) due to reduced electrolyte decomposition and improved structural stability of the cathode [16]. Recently, Peng et al. reported a high-capacity, long-life FeF_3 solid state battery based on sulfide-based Li_6PS_5Cl solid electrolyte [66, 67]. Nevertheless, challenges remain for room temperature operation of polymer-based solid state batteries because of the low ionic conductivity of polymer electrolyte. While a large capacity was achieved for FeF_3 cathode in sulfide-based solid-state batteries, most of the capacity is delivered at a much lower voltage than the theoretical electrode potential of FeF_3 [68], suggesting possible side reaction between FeF_3 with the sulfide electrolytes. Recently, Shao et al. reported the utilization of halide-based Li_3YCl_6 solid electrolyte can enable a complete conversion and reconversion of FeF_2 cathode at its theoretical potential due to the excellent (electro)chemical stability between Li_3YCl_6 and FeF_2 cathode [69]. Solid state FeF_2 cathode based on Li_3YCl_6 solid electrolyte also delivered excellent cycling stability with a low voltage hysteresis, suggesting a promising approach to address the performance limitation of iron fluoride cathodes.

In this work, we aim to understand the role of CuF_2 and NiF_2 incorporation in the electrochemical performance of FeF_3 cathodes with halide-based Li_3YCl_6 solid electrolyte. The fundamental question we would like to answer is whether we can achieve the kinetic benefits of cation incorporation in FeF_3, which has a higher energy density than FeF_2, while suppressing transition metal dissolution and interphase growth by solid-state concept to simultaneously lower voltage hysteresis and improve cycle life. Combining electrochemical analysis and material characterization, we report that the incorporation of CuF_2 and NiF_2 in FeF_3 cathode does not have an apparent effect in improving the electrode kinetics in Li_3YCl_6-based solid state batteries. However, apparent improvement in cycling stability of the FeF_3 can be achieved probably due to the suppression of transition metal

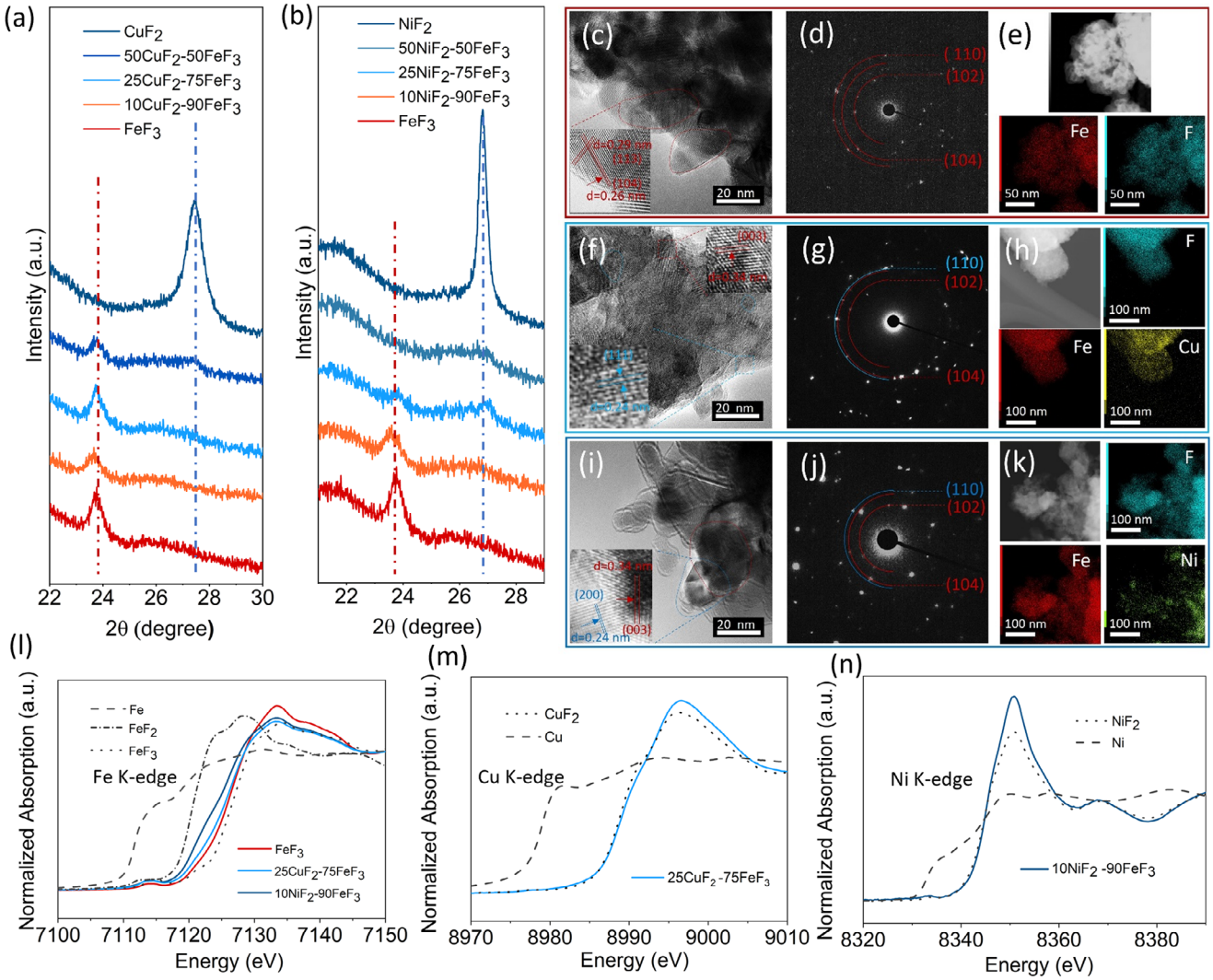

FIGURE 1 | XRD patterns of CuF_2-FeF_3 (a) and NiF_2-FeF_3 (b). HRTEM image, SAED, and elemental mapping of FeF_3 (c to e), $25CuF_2$-$75FeF_3$ (f–h), and $10NiF_2$-$90FeF_3$ (i to k). (l) Fe K-edge XANES spectra of FeF_3, $25CuF_2$-$75FeF_3$, and $10NiF_2$-$90FeF_3$. (m) Cu K-edge XANES spectra of $25CuF_2$-$75FeF_3$. (n) Ni K-edge XANES spectra of $10NiF_2$-$90FeF_3$.

dissolution and improvements in the mechanical stability of the cathodes.

2 | Results and Discussion

2.1 | Characterizations of FeF_3, CuF_2-FeF_3, and NiF_2-FeF_3

The incorporation of CuF_2 and NiF_2 in FeF_3 is achieved by high-energy ball-milling of CuF_2 and NiF_2 with FeF_3 with various molar contents of CuF_2/NiF_2 from 0% to 100%. The same method was also used to prepare ternary transitional metal fluoride solid solutions [19]. Cu and Ni were chosen as the incorporated cations because the high electrode potential (3.55 V for CuF_2 and 2.96 V for NiF_2) and theoretical capacity (528 mAh/g for CuF_2 and 554 mAh/g for NiF_2) [12, 26] to ensure that the potential improvements in kinetics and cycling performance do not largely compromise the energy density. Figure 1a,b shows the XRD patterns of CuF_2 and NiF_2 incorporated FeF_3. Significant peak broadening can be observed for all samples containing FeF_3, suggesting a reduction in particle sizes during high-energy ball-milling (Figure S1). Bragg reflections of FeF_3 (ReO_3-type structure, space group $R\bar{3}c$) and CuF_2 (monoclinic, space group $P2_1/n$)/NiF_2 (tetragonal, space group $P4_2/mmm$) can be observed for all mixed fluorides with no impurity phases. No apparent peak shift can be observed for each phase. The results suggest the CuF_2-FeF_3 and NiF_2-FeF_3 are most likely nanocomposites of the difluoride and FeF_3, instead of substitution. It should be noted that a rutile-like Cu-Fe-F compound with the oxidation state of Cu and Fe being +2 and +3, respectively, was reported as the product after charging $Cu_{0.5}Fe_{0.5}F_2$ solid solution to 4.5 V [19]. Such a rutile compound is not observed in the XRD results.

HRTEM was used to probe the structure of FeF_3, $25CuF_2$-$5FeF_3$, and $10NiF_2$–$90FeF_3$ (Figure 1c–k). All three mixed fluorides show agglomeration of highly crystalline nanoparticles with a size of 5–10 nm (Figure 1c,f,i). Lattice fringes with interplanar spacing corresponding to FeF_3, CuF_2, and NiF_2 can be observed in the mixed fluorides. The presence of CuF_2 and NiF_2 in the

mixed fluorides is also confirmed from the selected area electron diffraction (SAED) (Figure 1d,g,j), consistent with the XRD results (Figure 1a,b) that the $25CuF_2$–$75FeF_3$ and $10NiF_2$–$90FeF_3$ are composites in nature. The composite feature of the mixed fluorides was also supported by the EDS results (Figure 1e,h,k), which show nonuniform distribution of Fe and Cu/Ni in $25CuF_2$–$75FeF_3$ and$10NiF_2$–$90FeF_3$. It should be noted that the particle size of CuF_2 was observed to be much smaller than FeF_3 and NiF_2, and this help explain the weak diffractions from both SAED (Figure 1h) and XRD (Figure 1a), although the molar content of CuF_2 in $25CuF_2$–$75FeF_3$ is higher than that of NiF_2 in $10NiF_2$–$90FeF_3$.

To understand the effect of CuF_2/NiF_2 incorporation on the electronic structure of transition metals, we also measured the synchrotron X-ray absorption near edge structure (XANES) of Fe K-edge (Figure 1l), Cu K-edge (Figure 1m), and Ni K-edge (Figure 1n) in FeF_3, $25CuF_2$–$75FeF_3$, and $10NiF_2$–$90FeF_3$. Reference XANES spectra of commercial metals (Fe, Cu, and Ni) and metal fluorides (FeF_2, FeF_3, CuF_2, and NiF_2) were also measured as reference. Although slight shift of the absorption edge to lower energies can be observed, the line shape of Fe K-edge XANES spectra in FeF_3, $25CuF_2$–$75FeF_3$, and $10NiF_2$–$90FeF_3$ are quite similar to that of the micron-sized FeF_3 (Figure 1l). The underlying reason for the slight shift of the absorption edge of Fe for $25CuF_2$–$75FeF_3$ and $10NiF_2$–$90FeF_3$ to a lower energy is currently unknown but might be due to slight doping of Fe into NiF_2/CuF_2, which can lead to slight reduction of Fe. The XANES spectra of Cu K-edge of $25CuF_2$–$75FeF_3$ (Figure 1m) and Ni K-edge of $10NiF_2$–$90FeF_3$ (Figure 1n) are also similar to that of CuF_2 and NiF_2 reference spectra, respectively, further confirming the mixed fluoride are largely composite in nature.

2.2 | Effect of CuF_2/NiF_2 Incorporation on the Electrochemical Performance of FeF_3

To measure the electrochemical performance, FeF_3, CuF_2–FeF_3, and NiF_2–FeF_3 were first mixed with vapor grown carbon fiber (VGCF) and then Li_3YCl_6 solid electrolytes, both by a ball-milling process, to make composite cathodes. The electrochemical performance of FeF_3, CuF_2–FeF_3 and NiF_2–FeF_3 composite cathodes were measured by galvanostatic cycling at various current densities in a solid-state cell with Li_3YCl_6 solid electrolyte and Li-In anode at 60°C. The active material loading for each cell is fixed at around 2.6 mg/cm^2. Figure 2a,b compares the charge/discharge curves for the second cycle of CuF_2–FeF_3 and NiF_2–FeF_3 cathodes with those of FeF_3 cathode. Two typical voltage plateaus, ~3.4–3.6 V and ~1.7 V during discharge and ~2.6 and ~3.7 V during charge can be observed in the charge/discharge profiles of FeF_3, as also shown in the cyclic voltammetry results (Figure S2). The specific capacity for is 693 mAh/g for discharge and 612 mAh/g for discharge. The reversible capacity is close to the theoretical capacity (712 mAh/g), although part of the capacity may be from the reversible decomposition of Li_3YCl_6 solid electrolyte as a higher reversible capacity can be observed for the first cycle (Figure S3). The incorporation of CuF_2 leads to decreases of overall capacity (Figure 2c). On the other hand, the incorporation of NiF_2 leads to decreases in the specific capacities in the high-voltage-plateau region, due to the reduced contribution from FeF_3 intercalation, and increase in the specific capacities of in the low-voltage-plateau region due to additional redox from NiF_2 conversion (Figure 2d). A much larger capacity decrease can be observed for CuF_2-FeF_3 cathodes than NiF_2-FeF_3 at the same molar contents. It should be noted that increasing the NiF_2 content does not lead to a proportional decrease in discharge capacity (Figure 2d), despite its lower theoretical capacity compared to FeF_3, possibly due to the role of NiF_2 conversion in promoting the utilization of FeF_3 during discharge, for example, by generating electrically conductive Ni prior to the conversion of FeF_2.

Nevertheless, we do not observe reduction in the voltage hysteresis after CuF_2/NiF_2 incorporation (Figure 2a,b). Both CuF_2-FeF_3 and NiF_2-FeF_3 showed a higher voltage hysteresis than FeF_3 (Figure S4). The results suggest that the kinetic benefits of mixed difluoride solid solutions in liquid electrolyte cannot be transferred to the mixed trifluoride nanocomposites. Nevertheless, the incorporation of CuF_2 and NiF_2 are beneficial to improve the cycling performance of FeF_3 cathode in Li_3YCl_6-based solid-state batteries (Figure 2c,d). The charge/discharge curves for the cycling performance tests at different current densities are shown in Figure S5. All NiF_2-containing cathodes showed improved cycling stability than FeF_3 cathode (Figure 2d). For CuF_2-containing cathodes, the cycling stability first increases and then decreases with CuF_2 content with FeF_3 cathode, with 25 mol% CuF_2 exhibiting the best cycling stability for the first 50 cycles (Figure 2c). Given the excellent performance of $10NiF_2$-$90FeF_3$ and $25CuF_2$-$75FeF_3$ cathodes, we then focused on these two cathodes to understand the effects of CuF_2/NiF_2 incorporation on the kinetics and cycling stability of FeF_3.

2.3 | Effect of CuF_2/NiF_2 Incorporation on the Reaction Mechanism of FeF_3 Cathodes

The electronic structure of the FeF_3, $25CuF_2$-$75FeF_3$, and $10NiF_2$-$90FeF_3$ cathode composites were probed by XANES spectra of Fe, Cu, and Ni K-edge. We first compared the XANES spectra of the composite cathodes with those of the FeF_3, $25CuF_2$-$75FeF_3$, and $10NiF_2$-$90FeF_3$ active materials (Figure 1l–n) to investigate the chemical stability between the active material and Li_3YCl_6 solid electrolyte during fabrication of the cathode composite through ball milling. For Fe-K edge, the absorption edge of XANES spectra of all pristine cathode composites (Figure 3a,b,d) shifted to a lower energy that corresponds to Fe^{2+}, suggesting the reduction of Fe from Fe^{3+} to Fe^{2+}. The reduction of Cu, to form Cu^+ species, can also be observed based on the shift of the absorption edge of Cu K edge (Figure 3c), while the oxidation state of Ni remains +2 in the $10NiF_2$-$90FeF_3$ (Figure 3e). The results suggest the instability of the FeF_3-based cathodes with Li_3YCl_6 solid electrolyte during cathode composite fabrication.

To understand the effect of CuF_2/NiF_2 incorporation in the reaction mechanism of FeF_3, we measured the XANES spectra of FeF_3, $10NiF_2$-$90FeF_3$, and $25CuF_2$-$75FeF_3$ composite cathodes at the fully discharged and fully charged states (Figure 3a–e). For FeF_3 cathode, after discharge to 1.0 V vs. Li/Li$^+$, the Fe K-edge XANES spectrum exhibits a pronounced shift of the absorption edge toward lower energy, accompanied by a substantial change in line shape (Figure 3a). The edge position and post-edge features approach those of metallic Fe, indicating a reduction of Fe^{2+} to Fe^0 during the conversion reaction. The oxidation of Fe from

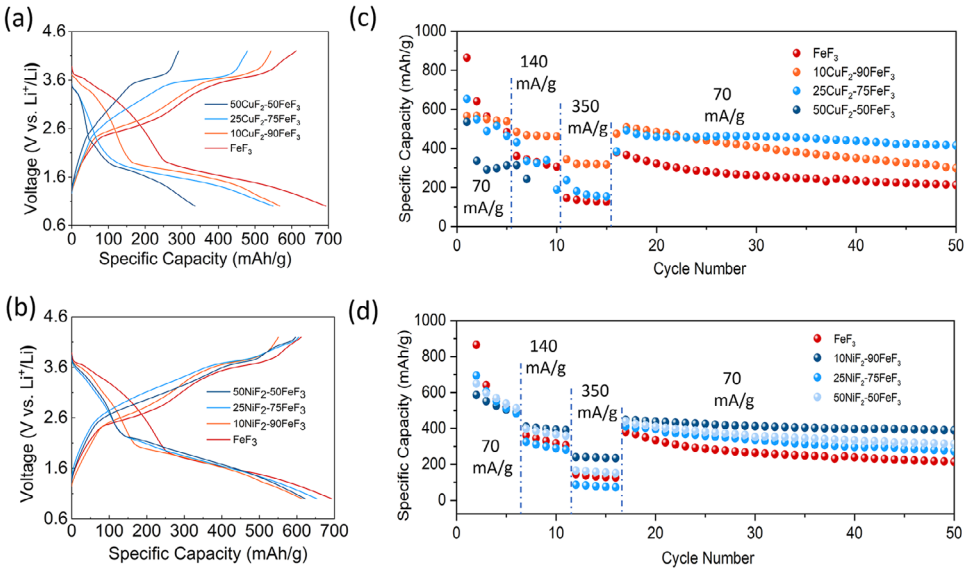

FIGURE 2 | Charge/discharge curves of CuF_2–FeF_3 (a) and NiF_2–FeF_3 (b) in Li_3YCl_6 based solid-state batteries at 70 mA/g. Cycling performance of CuF_2–FeF_3 (c) and NiF_2–FeF_3 (d) in Li_3YCl_6-based solid-state batteries at various current densities. Li-In was used as the anode, and the electrochemical performances were measured at 60°C.

Fe^0 to Fe^{3+} can be observed after charging to 4.2 V, based on the shift of the absorption edge to a higher energy (Figure 3a). However, comparing the line shape of the spectrum with the XANES spectra of $FeCl_3$ and FeF_3 reference samples, Fe in the fully charged electrode mainly exists as $FeCl_3$, rather than FeF_3, indicating that the electrochemical reaction between FeF_3 and Li_3YCl_6 also occurred during the charge/discharge processes. The results are consistent with a prior study that reports a large content of $FeCl_3$ after charging FeF_2-Li_3YCl_6 cathode to 4.0 V vs. Li/Li^+ [69]. Complete reduction from Fe^{2+} to Fe° can also be observed in the $25CuF_2$-$75FeF_3$ and $10NiF_2$-$90FeF_3$ composite cathodes. However, after charging, Fe in $25CuF_2$-$75FeF_3$ will be oxidized to Fe^{2+} in the form of $FeCl_2$ (Figure 3b) while for $10NiF_2$-$90FeF_3$ the Fe will be oxidized to $FeCl_3$ with an oxidation state of +3 (Figure 3d). The formation of $FeCl_3$ is believed to be reversible due to the very similar charge profile of the second cycle when compared with that of the first cycle. The evolution of XANES of Cu K-edge (Figure 3c) indicates the reduction of Cu^+ to Cu^0 after discharge and the oxidation of Cu^0 to Cu^+ after charge. Interestingly, the absorption edge of XANES of Cu K-edge for the fully charged $25CuF_2$-$75FeF_3$ appears at a lower energy than that of the pristine sample (Figure 3c), which is likely due to the change in the local environment of Cu^+ from CuF-like species in the pristine electrode to CuCl-like species in the fully charged electrode. The XANES spectra of Ni K-edge (Figure 3e) show a reduction from NiF_2 to Ni during discharge and oxidation back to NiF_2 during charge, indicative of a complete conversion and reconversion of NiF_2 during charge/discharge process.

The above XAS analysis highlights the complexity of the chemical and electrochemical stability between the FeF_3-based cathodes and Li_3YCl_6 solid electrolytes. The results show clear involvement of Cu and Ni redox processes during charge and discharge process and indicate the significant role of electrochemical stability of Li_3YCl_6 in the reaction pathway of the FeF_3-based cathodes. Complete oxidation from Fe^0 to Fe^{3+} can be achieved in FeF_3 and $10NiF_2$-$90FeF_3$, while in $25CuF_2$-$75FeF_3$ Fe° can only be oxidized to Fe^{2+} at the fully charged states. The results also help explain the slightly lower discharge plateau of $25CuF_2$-$75FeF_3$ than that of FeF_3 and $10NiF_2$-$90FeF_3$ for the second cycle (Figure 2; Figure S2). For FeF_3 and $10NiF_2$-$90FeF_3$, the high voltage plateau is mainly attributed to the reduction of Fe^{3+} to Fe^{2+} while in CuF_2-FeF_3 it is related to the reduction of Cu^+. The low-voltage plateau, however, for all three electrodes, can be attributed to the reduction of Fe^{2+} to Fe^0.

2.4 | Effect of CuF_2/NiF_2 Incorporation on Electrode Kinetics of FeF_3 Cathodes

To understand the effect of cation incorporation on electrode kinetics, we also performed galvanostatic intermittent titration technique (GITT) of the cathodes during the second cycle. The quasi-equilibrium voltage profiles, shown in the shaded region, show low voltage hysteresis for all three cathodes (Figure 4a–c), suggesting the voltage hysteresis for these cathodes in Li_3YCl_6-based solid-state batteries is kinetic in nature. The kinetics of the electrode can be reflected by the overpotential, which is the difference of the potential before and after rest, during charge and discharge (Figure S6). Figure 4d compares the evolution of overpotential during charge and discharge of the second cycle. All three cathodes show similar trend with the depth of discharge (DOD). The overpotentials first increase when the electrodes are discharged to 30% DOD, decrease to 45%, increase to 80%, and then slightly decrease until 100% DOD. A similar trend was also observed in previous GITT study of FeF_3 electrode in liquid electrolyte [11, 14]. The largest overpotential is observed at around the transition point between high-voltage-plateau and low-voltage plateau, and this is probably attributed to the kinetic barrier for nucleation Fe and LiF. During charge, the overpotential first increase to the maximum, decrease at around 80% SOC with a slight increase until the end of charge. Comparing the magnitude of the overpotential, $25CuF_2$–$75FeF_3$ shows the largest overpotential across the states of charge, while $10NiF_2$–$90FeF_3$

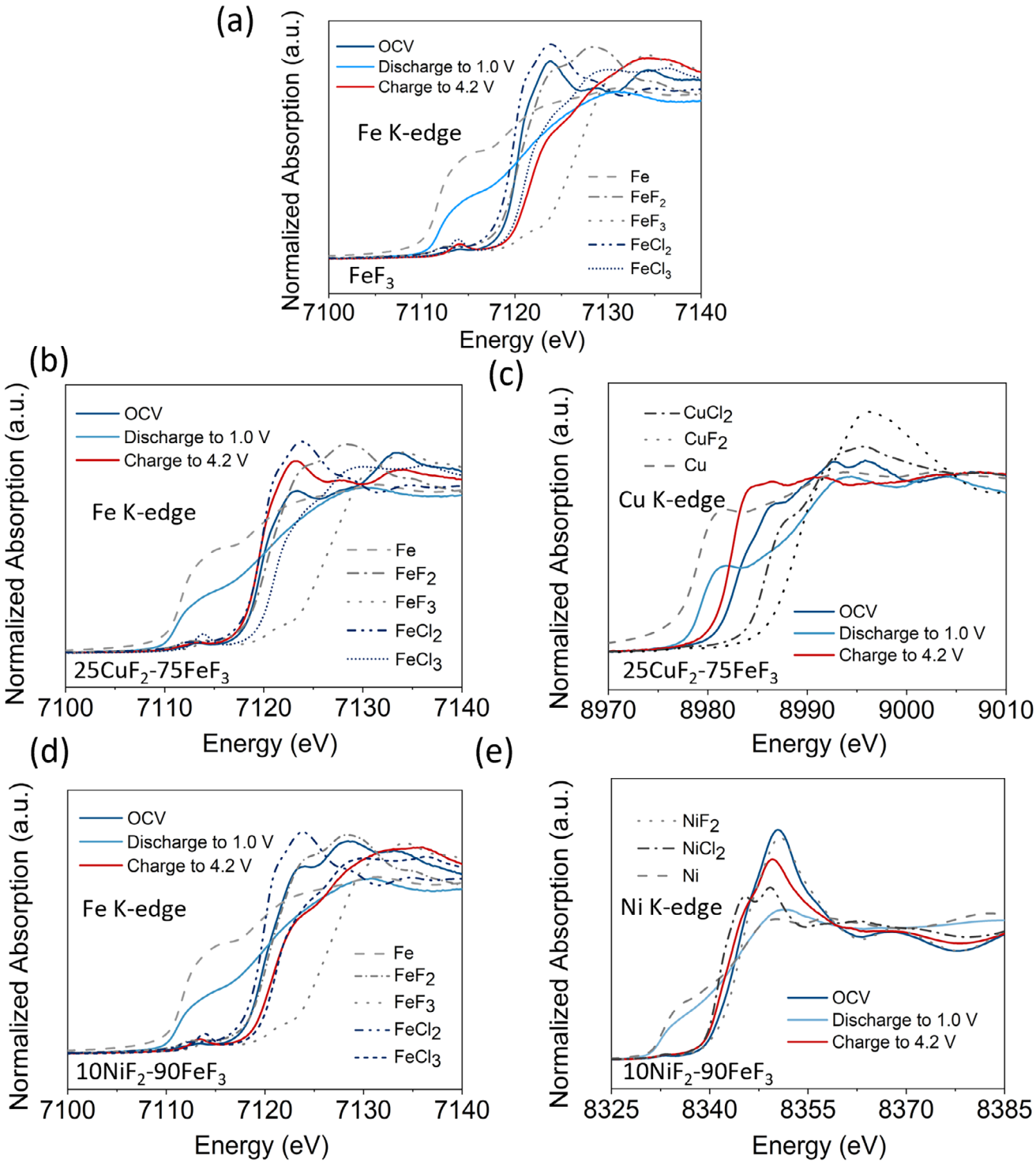

FIGURE 3 | Near-edge XAS spectra (XANES) for the Fe K-dege, Cu K-dege and Ni K-edge of FeF_3, $25CuF_2$–$75FeF_3$, and $10NiF_2$–$90FeF_3$ electrodes after discharge and charge.

exhibit a slight lower but comparable overpotential with that of FeF_3.

To further validate the kinetic analysis through GITT, we also calculated the distribution of relaxation times (DRT) based on the electrochemical impedance spectra (Figures S7–S9) for FeF_3, $25CuF_2$–$75FeF_3$, and $10NiF_2$–$90FeF_3$ during discharge and charge of the second cycle. Figure 4e,f shows the 2D DRT map of the cathodes. Based on the DRT result of a Li-In|LYC|Li-In reference cell (Figure S10), the cathode/electrolyte interfacial resistance can be represented by the peak at a characteristic time of 1 s. The results from DRT are consistent with the GITT analysis (Figure 4d). Similar asymmetry of the kinetics for charge and discharge can be observed based on the evolution of the impedance corresponding to a characteristic time of 1s in Figure 4e,f. Incorporating CuF_2 in FeF_3 led to large increases in the cathode/electrolyte interfacial

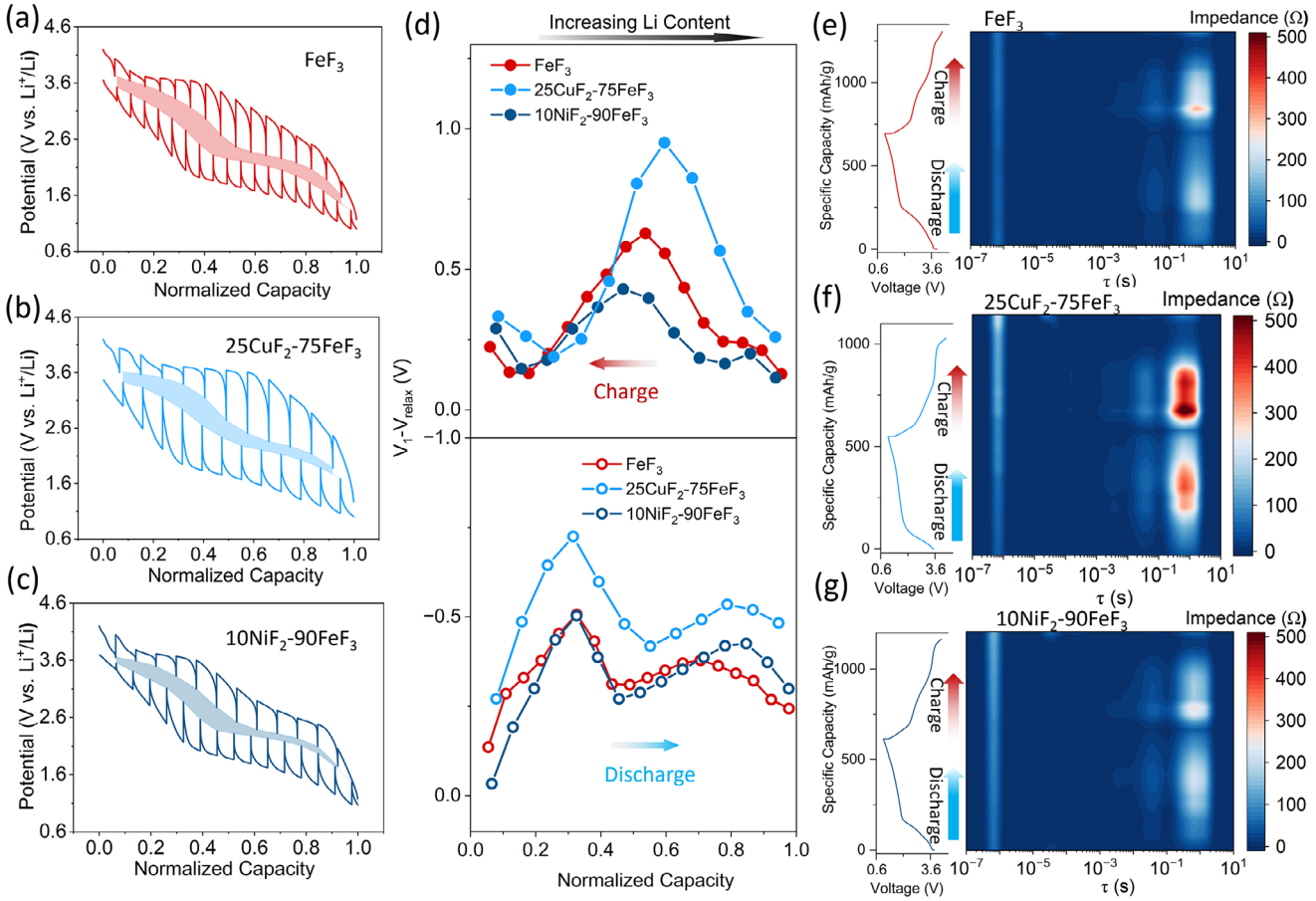

FIGURE 4 | GITT analysis of FeF_3 (a), $25CuF_2$–$75FeF_3$ (b), $10NiF_2$–$90FeF_3$ (c) during discharge and charge for the second cycle. (d) Evolution of the overpotential, determined from the GITT measurement, during charge and discharge. 2D DRT surface of FeF_3 (e), $25CuF_2$–$75FeF_3$ (f), and $10NiF_2$–$90FeF_3$ (g) during charge and discharge for the second cycle.

resistances, although a slight lower impedance can be observed for the $10NiF_2$-$90FeF_3$ cathode. The results further validate that the incorporation of Cu and Ni cannot effectively improve the kinetics of FeF_3 cathodes.

Correlating with the XANES results, we believe the more sluggish kinetics for $25CuF_2$–$75FeF_3$ is primarily due to the difference in the reaction mechanisms. While the low-voltage plateau for all three cathodes corresponds to oxidation of Fe to Fe^{2+}, the reaction mechanisms for the high voltage plateau are different. For FeF_3 and $10NiF_2$-$90FeF_3$, it is attributed of oxidation of Fe^{2+} to Fe^{3+} and Ni to Ni^{2+} but is corresponding to oxidation of Cu to Cu^+ for $25CuF_2$–$75FeF_3$. We suspect the origin of the sluggish kinetics of $25CuF_2$–$75FeF_3$ is attributed to the large particle of Cu, given that Cu has a more apparent coarsening effect than Ni and Fe due to its higher homologous temperature at the testing temperature (60°C). Despite that, no apparent feature of Cu° can be observed in the Cu K-edge XANES of the fully charged CuF_2-FeF_3 cathode, suggesting that even though the kinetics is sluggish, all Cu° can be oxidized, which is sharply different from the results in liquid electrolytes where residual Cu° can be observed for the charging CuF_2-FeF_3 cathode even to 4.5 V vs. Li/Li^+ [19]. The result implies that the utilization of solid electrolytes may suppress the growth of Cu nanoparticles compared to liquid electrolytes, i.e., although Cu still grows, it does not grow as fast as in liquid electrolyte batteries. Another possible reason for the different electrode kinetics in solid state and liquid electrolyte batteries might be related to Cu dissolution. While dissolution is not desired for improving cycling stability, it can help reaction kinetics, such as in liquid-electrolyte lithium sulfur batteries, especially given that the conversion reaction of CuF_2 is topotactic transformation in nature involving the transport of both Li and Cu [25].

2.5 | Effect of CuF_2/NiF_2 Incorporation on Cycling Stability of FeF_3 Cathodes

Although no apparent improvement in kinetics can be observed, we did observe a large improvement in the cycling stability after CuF_2/NiF_2 incorporation (Figure 2c,d). The improvement in the cycling performance was further validated by long-cycling tests of FeF_3, $25CuF_2$–$75FeF_3$, and $10NiF_2$–$90FeF_3$ at 0.5 C (Figure 5a). $25CuF_2$–$75FeF_3$ demonstrates the best cycling stability with minimal capacity decay for more than 100 cycles. It has been reported that the incorporation of NiF_2 into FeF_2 led to quick capacity decay for the first 25 cycles in liquid electrolyte batteries due to the significant growth of cathode electrolyte interphase [21, 23], and Cu-containing FeF_2 can be cycled for a few times in liquid electrolyte due to Cu dissolution [19, 55]. While a fast capacity decay can also be observed in solid-state cells for the first few cycles (Figure 5a) arising from microstructural and interphase stabilization due to the (electro)chemical instability between the

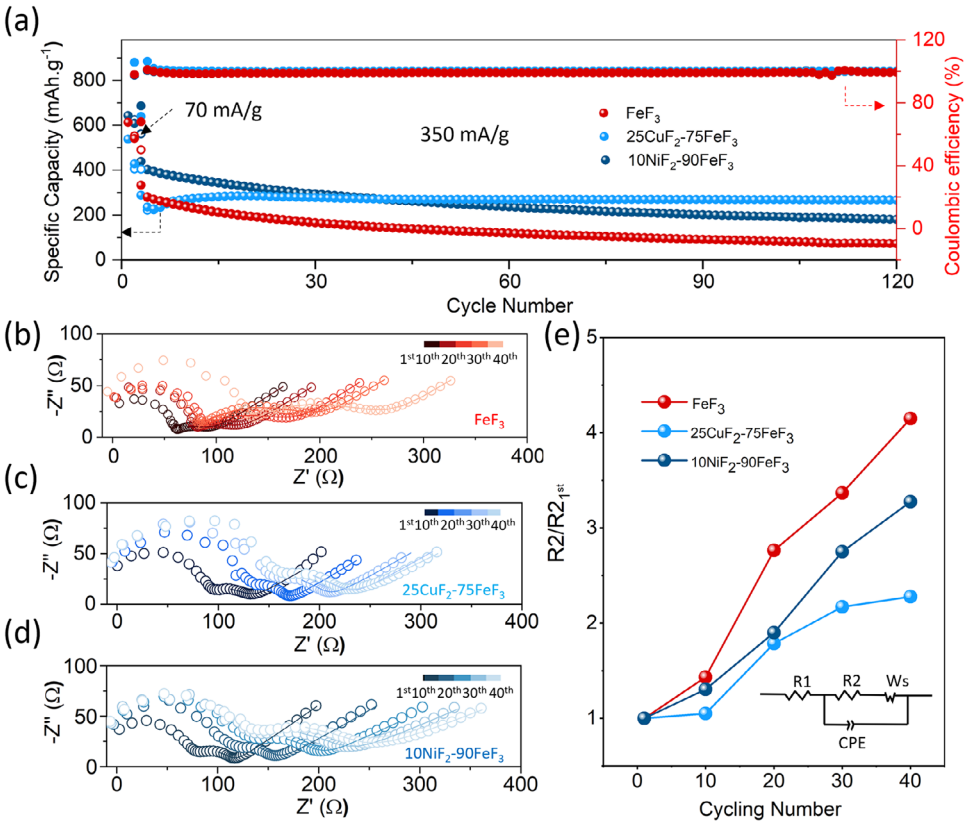

FIGURE 5 | (a) Cycling performance and coulombic efficiency of FeF_3, $25CuF_2$–$75FeF_3$, and $10NiF_2$–$90FeF_3$. (b–d) Nyquist plots collected from the first to the 100th cycle at intervals of 10 cycles, showing progressive impedance growth for FeF_3 (b), $25CuF_2$–$75FeF_3$ (c), and $10NiF_2$–$90FeF_3$ (d). (e) Cathode/electrolyte impedances after cycling 10, 20, 30, and 40 times.

solid electrolyte and the electrodes, the capacity can quickly stabilize for the first few cycles. The cycling performances of solid state $25CuF_2$–$75FeF_3$ and $10NiF_2$–$90FeF_3$ cathode represent a significant improvement, suggesting the advantages of using solid electrolyte to improve the cycling performance by forming a less dynamic interphase and eliminating transition metal dissolution. It should be noted that the less dynamic feature of the interphase formation in solid-state batteries mainly arise from the elimination of continuous reformation of the interphase upon cracking or pulverization due to non-infiltrative features of solid electrolytes compared to liquids. However, it does not suggest that the solid electrolyte will be more (electro)chemically stable with the electrode than liquid electrolytes. The (electro)chemical instability between Li_3YCl_6 and FeF_3-basaed solid electrolyte also led to irreversible formation of LiF that remains in the cathode composite, and the existence of LiF may play a role in stabilizing the interface due to its excellent stability. The average coulombic efficiency of FeF_3, $25CuF_2$-$75FeF_3$, and $10NiF_2$-$90FeF_3$ during long-term cycling are 99.1%, 100.0%, and 99.6%, respectively. The results suggest that the incorporation of CuF_2 and NiF_2 helps to improve the reversibility during charge and discharge, which in turn leads to an enhanced cycling stability of the cathode. The high coulombic efficiencies for all three cathodes also suggest the stability of the interphase after it was formed for the first few cycles.

The excellent cycling performance after CuF_2/NiF_2 incorporation is also supported by the impedance evolution after different cycles (Figure 5b–d). The second semicircle corresponds to the interfacial resistance between cathode and solid electrolyte. While the initial cathode/electrolyte interfacial resistance of FeF_3 (12.9 Ω) is lower than that of $25CuF_2$–$75FeF_3$ (55.7 Ω) and $10NiF_2$–$90FeF_3$ (39.6 Ω) due to its better kinetics for the first few cycles, as also demonstrated in the GITT and DRT analysis (Figures 4 and 5), it increases faster during long-term cycling. The increase rate of the impedance is consistent with the cycling performance, with the $25CuF_2$–$75FeF_3$ exhibiting the lowest impedance increase for the first 40 cycles.

The exact mechanism for the enhanced cycling stability after CuF_2/NiF_2 incorporation is currently unknown but may be related to the mitigated electro-chemo-mechanical degradation, which has been considered as one key source for the cycling instability of solid-state electrodes [70–72]. The incorporation of CuF_2 and NiF_2 can lead to multiple redox centers occurring at different voltage, and more importantly at different locations of the electrodes, depending on the distribution of transition metals in the electrode. Instead of lithiation or delimitation between Fe^0 and Fe^{3+} at a single site, the capacity of the electrode can be achieved by redox behavior at different sites and potentials. Such corporative redox behavior will help reduce the strain/stress generated in the electrode composite, thus mitigating the contact loss due to the electro-chemo-mechanical degradation during long term cycling. Similar concept has been demonstrated in mixed transition metal oxide for conversion anodes [73]. More careful characterizations to understand the pressure evolution during long term charge/discharge cycles and to correlate it with the microstructure evolution especially at the cathode/electrolyte

interfaces would be very helpful to validate this mechanism. Additional mechanisms that may help improve the cycling stability include the formation of more passivating interphase after incorporating CuF_2/NiF_2, which is supported by the improve coulombic efficiency during long-term cycling.

3 | Conclusions

We investigated the effect of CuF_2 and NiF_2 incorporation in electrochemical performance of FeF_3 cathodes in Li_3YCl_6-based solid-state batteries. The difference in the structure of CuF_2/NiF_2 and FeF_3 led to the formation of a nanocomposite of these fluorides. Different from the previous report on the enhanced electrode kinetics of ternary metal fluorides in liquid electrolyte batteries, no apparent decrease in voltage hysteresis can be observed after incorporation of CuF_2 or NiF_2 in FeF_3 in solid-state batteries. The XANES results confirmed the involvement of Cu (Cu^0/Cu^+) and Ni (Ni^0/Ni^{2+}) redox behaviors in the mixed fluorides. While the oxidation of Fe from Fe^0 to Fe^{3+} can be observed for FeF_3 and $10NiF_2$-$90FeF_3$ after charging to 4.2 V vs. Li/Li^+, only Fe^{2+} can be observed in fully charged CuF_2-FeF_3. The results suggest the complex reaction mechanisms of solid-state FeF_3, $25CuF_2$-$75FeF_3$, and $10NiF_2$-$90FeF_3$ electrodes, involving significant (electro)chemical reactions with Li_3YCl_6 solid electrolytes. The effect of CuF_2/NiF_2 incorporation on electrode kinetics was also studied by GITT and DRT analysis. While $10NiF_2$-$90FeF_3$ demonstrated comparable kinetic performance with FeF_3, the overpotential and impedance of $25CuF_2$-$75FeF_3$ are much higher, probably due to the different reaction mechanisms of these mixed fluorides. Nevertheless, significant improvement in the cycling performance can be observed after incorporating CuF_2 and NiF_2 in FeF_3, likely due to the mitigation of electro-chemo-mechanical degradations from the cooperative redox behavior of additional transition metal in solid-state batteries. The work highlights the unique advantages of using solid state concept to improve the cycling performance of FeF_3 cathodes and provides novel insights for developing FeF_3 cathodes for solid-state batteries.

4 | Experimental Section

4.1 | Materials Synthesis

Commercial FeF_3 (≥97%, Sigma–Aldrich), NiF_2 (≥99%, Alfa Aesar), and CuF_2 (≥99%, Sigma–Aldrich) were used as starting materials without further purification. NiF_2–FeF_3 and CuF_2–FeF_3 composites were prepared by high-energy ball milling. Specifically, stoichiometric amounts of FeF_3 and NiF_2 (or CuF_2) were weighed according to the desired molar ratios (10:90, 25:75, 50:50), sealed in a stainless steel jar with 10 balls under an Ar-filled glovebox, and milled at 300 rpm for 12 h with a ball-to-powder weight ratio of 60:1. The resulting powders were collected and stored in an argon atmosphere to prevent moisture uptake.

4.2 | Materials Characterization

Powder X-ray diffraction (XRD, Panalytical Empyrean, Cu Kα radiation) was used to analyze phase structures. Scanning electron microscopy (SEM, Carl Zeiss Supra 55) coupled with energy-dispersive X-ray spectroscopy (EDX) was employed to examine morphology and elemental distribution. Transmission electron microscopy (TEM) and high-resolution/atomic-resolution TEM (JEOL F200) were used to investigate microstructure, lattice fringes, and nanoscale elemental distribution. The K-edge XAS spectra of Fe, Cu, and Ni were measured in fluorescence mode at 7-BM beamline (QAS) of National Synchrotron Light Source II (NSLS II), Brookhaven National Laboratory (BNL), using standard references (Fe, FeF_2, FeF_3, Ni, NiF_2, Cu, CuF_2) for comparison. The data was analyzed using the Athena software.

4.3 | Electrochemical Measurements

Composite cathodes were prepared by mixing active material (FeF_3 or NiF_2/CuF_2–FeF_3 composite), vapor-grown carbon fibers (VGCF), and Li_3YCl_6 (LYC) in a weight ratio of 4:2:4. LYC is also prepared by ball milling at 500 rpm for 55 h in ZrO_2 jars with a ball-to-powder weight ratio of 30:1 as we reported in the previous work [69, 74]. The mixture was prepared by ball milling with active materials and VGCF at 380 rpm for 10 h and then with LYC at 360 rpm for 1.5 h. All-solid-state cells were assembled in an Ar-filled glovebox (<0.1 ppm O_2 and H_2O). The LYC (120 mg) was pressed into pellets (diameter 10 mm) under 100 MPa for 3 min. The cathode layer (5 mg) was uniformly spread on one side of the pellet under 300 MPa for 3 min, followed by an In–Li alloy powder anode on the other side (500 mg). The stacked cell was pressed under 350 MPa for 1 min to ensure intimate contact. Galvanostatic charge–discharge cycling was carried out using a LAND battery tester in the voltage range of 1.0–4.2 V (vs. Li^+/Li). Rate performance was tested at current densities of 70, 140, and 350 mA/g, followed by recovery at 0.1 C (1 C = 712 mAh/g). The GITT test was conducted by applying a constant current of 0.1424 mA/g for 30 min, followed by an open-circuit relaxation for 10 h using an Arbin system. EIS spectra at each relaxation step during the GITT test using a Gamry instrument. At each potential step, the cell was held for 5 h to reach a quasi-steady state before applying an AC perturbation over the frequency range of 10 MHz to 0.01 Hz. CV was measured on a Bio-Logic VMP3 potentiostat at a scan rate of 0.01 mV s^{-1}.

Author Contributions

Fudong Han conceived the idea and supervised the project. K.X. prepared the materials, performed the electrochemistry tests, and conducted the XRD, SEM, and EDX analysis. Ru Xiao assisted with the DRT analysis. K.X. and Enyuan Hu performed the XAS tests. K.X. and Fudong Han wrote the manuscript with the input of all the co-authors.

Acknowledgements

K.X., R.X., G.R., R.D., R.W., R.D, B.S., and F.H. acknowledge support from the US Department of Energy (DOE), Advanced Research Projects Agency for Energy (ARPA-E), IGNIITE program (Award No. DE-AR0001927). K.X., and E.H. are supported by the Assistant Secretary for Energy Efficiency and Renewable Energy, Vehicle Technology Office of the US Department of Energy through the Advanced Battery Materials Research (BMR) Program under contract no. DE-SC0012704. This research used beamline 7-BM (QAS) of the National Synchrotron Light Source II, U.S. DOE Office of Science User Facilities, operated for the DOE Office of Science by Brookhaven National Laboratory under contract no. DE-SC0012704.

Funding

K.X, R.X, G.R, R.D, R.W, R.D, B.S, and F.H. acknowledge support from the US Department of Energy (DOE), Advanced Research Projects Agency for Energy (ARPA-E), IGNIITE program (Award No. DE-AR0001927). K.X., and E.H. are supported by the Assistant Secretary for Energy Efficiency and Renewable Energy, Vehicle Technology Office of the US Department of Energy through the Advanced Battery Materials Research (BMR) Program under contract no. DE-SC0012704.

Conflicts of Interest

None of the authors have a conflict of interest to disclose.

Data Availability Statement

The data that support the findings of this study are available from the corresponding author upon reasonable request.

References

1. V. Viswanathan, A. H. Epstein, Y.-M. Chiang, et al., "The Challenges and Opportunities of Battery-Powered Flight," *Nature* 601 (2022): 519–525, https://doi.org/10.1038/s41586-021-04139-1.

2. J. Janek and W. G. Zeier, "A Solid Future for Battery Development," *Nature Energy* 1 (2016): 16141, https://doi.org/10.1038/nenergy.2016.141.

3. P. Poizot, S. Laruelle, S. Grugeon, L. Dupont, and J. Tarascon, "Nano-Sized Transition-Metal Oxides as Negative-Electrode Materials for Lithium-Ion Batteries," *Nature* 407 (2000): 496–499, https://doi.org/10.1038/35035045.

4. F. Badway, F. Cosandey, N. Pereira, and G. G. Amatucci, "Carbon Metal Fluoride Nanocomposites," *Journal of The Electrochemical Society* 150 (2003): 1318–1327, https://doi.org/10.1149/1.1602454.

5. F. Badway, N. Pereira, F. Cosandey, and G. G. Amatucci, "Carbon-Metal Fluoride Nanocomposites: Structure and Electrochemistry of FeF_3: C," *Journal of the Electrochemical Society* 150 (2003): A1209–A1218.

6. H. Li, P. Balaya, and J. Maier, "Li-Storage via Heterogeneous Reaction in Selected Binary Metal Fluorides and Oxides," *Journal of the Electrochemical Society* 151 (2004): A1878–A1885.

7. R. E. Doe, K. A. Persson, Y. S. Meng, and G. Ceder, "First-Principles Investigation of the Li–Fe–F Phase Diagram and Equilibrium and Nonequilibrium Conversion Reactions of Iron Fluorides With Lithium," *Chemistry of Materials* 20 (2008): 5274–5283, https://doi.org/10.1021/cm801105p.

8. N. Yamakawa, M. Jiang, B. Key, and C. P. Grey, "Identifying the Local Structures Formed During Lithiation of the Conversion Material, Iron Fluoride, in a Li Ion Battery: A Solid-State NMR, X-Ray Diffraction, and Pair Distribution Function Analysis Study," *Journal of the American Chemical Society* 131 (2009): 10525–10536, https://doi.org/10.1021/ja902639w.

9. J. Cabana, L. Monconduit, D. Larcher, and M. R. Palacín, "Beyond Intercalation-Based Li-Ion Batteries: The State of the Art and Challenges of Electrode Materials Reacting Through Conversion Reactions," *Advanced Materials* 22 (2010): E170–E192, https://doi.org/10.1002/adma.201000717.

10. S. W. Kim, D. H. Seo, H. Gwon, J. Kim, and K. Kang, "Fabrication of FeF_3 Nanoflowers on CNT Branches and Their Application to High Power Lithium Rechargeable Batteries," *Advanced Materials* 22 (2010): 5260–5264, https://doi.org/10.1002/adma.201002879.

11. P. Liu, J. J. Vajo, J. S. Wang, W. Li, and J. Liu, "Thermodynamics and Kinetics of the Li/FeF_3 Reaction by Electrochemical Analysis," *The Journal of Physical Chemistry C* 116 (2012): 6467–6473, https://doi.org/10.1021/jp211927g.

12. F. Wu and G. Yushin, "Conversion Cathodes for Rechargeable Lithium and Lithium-Ion Batteries," *Energy & Environmental Science* 10 (2017): 435–459, https://doi.org/10.1039/C6EE02326F.

13. F. Wang, H. C. Yu, M. H. Chen, et al., "Tracking Lithium Transport and Electrochemical Reactions in Nanoparticles," *Nature Communications* 3 (2012): 1201, https://doi.org/10.1038/ncomms2185.

14. L. Li, R. Jacobs, P. Gao, et al., "Origins of Large Voltage Hysteresis in High-Energy-Density Metal Fluoride Lithium-Ion Battery Conversion Electrodes," *Journal of the American Chemical Society* 138 (2016): 2838–2848, https://doi.org/10.1021/jacs.6b00061.

15. S. Kim, J. Liu, K. Sun, J. Wang, S. J. Dillon, and P. V. Braun, "Improved Performance in FeF_2 Conversion Cathodes Through Use of a Conductive 3D Scaffold and Al_2O_3 ALD Coating," *Advanced Functional Materials* 27 (2017): 1702783, https://doi.org/10.1002/adfm.201702783.

16. Q. Huang, K. Turcheniuk, X. Ren, et al., "Cycle Stability of Conversion-Type Iron Fluoride Lithium Battery Cathode at Elevated Temperatures in Polymer Electrolyte Composites," *Nature Communications* 18 (2019): 1343–1349.

17. H. Jo, M. Gong, S. Y. Kim, D.-H. Seo, and S.-K. Jung, "Guided Phase Transition for Mitigating Voltage Hysteresis of Iron Fluoride Positive Electrodes in Lithium-Ion Batteries," *Nature Communications* 16 (2025): 8596, https://doi.org/10.1038/s41467-025-63676-9.

18. H. Hori and S. Okada, "Reconversion Reaction of LiF/Fe Composite Thin Film Cathodes for Lithium-Ion Battery," *Electrochemistry* 83 (2015): 909–913, https://doi.org/10.5796/electrochemistry.83.909.

19. F. Wang, S. W. Kim, D. H. Seo, et al., "Ternary Metal Fluorides as High-Energy Cathodes With Low Cycling Hysteresis," *Nature Communications* 6 (2015): 6668, https://doi.org/10.1038/ncomms7668.

20. X. Fan, E. Hu, X. Ji, et al., "High Energy-Density and Reversibility of Iron Fluoride Cathode Enabled via an Intercalation-Extrusion Reaction," *Nature Communications* 9 (2018): 2324, https://doi.org/10.1038/s41467-018-04476-2.

21. D. Gordon, Q. Huang, A. Magasinski, A. Ramanujapuram, N. Bensalah, and G. Yushin, "Mixed Metal Difluorides as High Capacity Conversion-Type Cathodes: Impact of Composition on Stability and Performance," *Advanced Energy Materials* 8 (2018): 1800213, https://doi.org/10.1002/aenm.201800213.

22. K. Karki, L. Wu, Y. Ma, et al., "Revisiting Conversion Reaction Mechanisms in Lithium Batteries: Lithiation-Driven Topotactic Transformation in FeF_2," *Journal of the American Chemical Society* 140 (2018): 17915–17922, https://doi.org/10.1021/jacs.8b07740.

23. Q. Huang, T. P. Pollard, X. Ren, et al., "Fading Mechanisms and Voltage Hysteresis in FeF_2–NiF_2 Solid Solution Cathodes for Lithium and Lithium-Ion Batteries," *Small* 2019, 15, 1804670.

24. A. W. Xiao, H. J. Lee, I. Capone, et al., "Understanding the Conversion Mechanism and Performance of Monodisperse FeF_2 Nanocrystal Cathodes," *Nature Materials* 19 (2020): 644–654.

25. X. Hua, A. S. Eggeman, E. Castillo-Martínez, et al., "Revisiting Metal Fluorides as Lithium-Ion Battery Cathodes," *Nature Materials* 20 (2021): 841–850, https://doi.org/10.1038/s41563-020-00893-1.

26. L. F. Olbrich, A. W. Xiao, and M. Pasta, "Conversion-Type Fluoride Cathodes: Current State of the Art," *Current Opinion in Electrochemistry* 30 (2021): 100779, https://doi.org/10.1016/j.coelec.2021.100779.

27. S. Tawa, K. Matsumoto, and R. Hagiwara, "Reaction Pathways of Iron Trifluoride Investigated by Operation at 363 K Using an Ionic Liquid Electrolyte," *Journal of The Electrochemical Society* 166 (2019): A2105–A2110, https://doi.org/10.1149/2.1151910jes.

28. L. Li, Y. C. K. Chen-Wiegart, J. Wang, et al., "Visualization of Electrochemically Driven Solid-State Phase Transformations Using Operando Hard X-Ray Spectro-Imaging," *Nature Communications* 6 (2015): 6883, https://doi.org/10.1038/ncomms7883.

29. W. Zhang, P. N. Duchesne, Z. L. Gong, et al., "In Situ Electrochemical XAFS Studies on an Iron Fluoride High-Capacity Cathode Material for Rechargeable Lithium Batteries," *The Journal of Physical Chemistry C* 117 (2013): 11498–11505, https://doi.org/10.1021/jp401200u.

30. Y. Meng, J. Hu, M. Lei, H. Wu, R. Qian, and C. Li, "Synergistic Lewis Acid and Hydrogen Bonding Strategy to Enable Polymerized and Wide-Temperature Li-Fe-F Conversion Solid-State Batteries," *Advanced Energy Materials* 15 (2025): 02645, https://doi.org/10.1002/aenm.202502645.

31. J. Hu, M. Lei, C. Zhu, B. Zhang, and C. Li, "Highly Conductive Doped Fluoride Solid Electrolytes With Solidified Ionic Liquid to Enable Reversible FeF_3 Conversion Solid State Batteries," *Advanced Functional Materials* 34 (2024): 2314044, https://doi.org/10.1002/adfm.202314044.

32. H. Wu, J. Hu, S. Yu, and C. Li, "Heterostructure Conductive Interface and Melt-Penetration-Bonding Process to Afford All-Solid-State Li–FeF_3 Garnet Batteries With high Cathode Loading," *Energy & Environmental Science* 18 (2025): 923–936, https://doi.org/10.1039/D4EE02947J.

33. F. Wang, R. Robert, N. A. Chernova, et al., "Conversion Reaction Mechanisms in Lithium Ion Batteries: Study of the Binary Metal Fluoride Electrodes," *Journal of the American Chemical Society* 133 (2011): 18828–18836, https://doi.org/10.1021/ja206268a.

34. Y. Gao, J. Li, Y. Hua, et al., "Recent Advances of Metal Fluoride Compounds Cathode Materials for Lithium Ion Batteries: A Review," *Materials Futures* 3 (2024): 032101, https://doi.org/10.1088/2752-5724/ad4572.

35. R. Wu, X. Bo, S. Zhao, et al., "Transition Metal Fluorides as Advanced Cathodes for Lithium/Sodium-Ion Batteries: Rational Enhancement Strategies and Underlying Electrochemical Mechanisms," *Advanced Functional Materials* 35 (2025): 2424603, https://doi.org/10.1002/adfm.202424603.

36. Y. N. Zhou, M. Sina, N. Pereira, et al., "$FeO_{0.7}F_{1.3}$/C Nanocomposite as a High-Capacity Cathode Material for Sodium-Ion Batteries," *Advanced Functional Materials* 25 (2015): 696–703, https://doi.org/10.1002/adfm.201403241.

37. W. Gu, O. Borodin, B. Zdyrko, et al., "Lithium–Iron Fluoride Battery With In Situ Surface Protection," *Advanced Functional Materials* 26 (2016): 1507–1516, https://doi.org/10.1002/adfm.201504848.

38. Q. Huang, K. Turcheniuk, X. Ren, et al., "Insights Into the Effects of Electrolyte Composition on the Performance and Stability of FeF_2 Conversion-Type Cathodes," *Advanced Energy Materials* 9 (2019): 1803323, https://doi.org/10.1002/aenm.201803323.

39. L. Ju, G. Wang, K. Liang, et al., "Significantly Improved Cyclability of Conversion-Type Transition Metal Oxyfluoride Cathodes by Homologous Passivation Layer Reconstruction," *Advanced Energy Materials* 10 (2020): 1903333, https://doi.org/10.1002/aenm.201903333.

40. M. Liu, B. Chen, T. Wu, et al., "rGO–Encapsulated Co/Ni Dual–Doped $FeF3_{0.33}H_2O$ Nanoparticles Enabling a High-Rate and Long-Life Iron (III) Fluoride–Lithium Battery," *Chemical Engineering Journal* 451 (2023): 138774, https://doi.org/10.1016/j.cej.2022.138774.

41. S. Luo, M. Gao, D. Cai, et al., "Thermodynamic Properties and Composites Design Principles of Metal Fluoride as Active Cathode Material for Lithium Batteries," *Journal of Energy Storage* 73 (2023): 108483, https://doi.org/10.1016/j.est.2023.108483.

42. T. Chen, H. Liu, M. Sun, et al., "Oxygen-Doped FeF_3 Nanosheets Prepared by the Liquid-Phase Exfoliation Method for Lithium Storage," *Energy & Fuels* 38 (2024): 12239–12250, https://doi.org/10.1021/acs.energyfuels.4c02072.

43. J. Park, Y. Yang, H. Park, et al., "Entropy-Stabilized Multication Fluorides as a Conversion-Type Cathode for Li-Ion Batteries–Impact of Element Selection," *ACS Applied Materials & Interfaces* 16 (2024): 57151–57161, https://doi.org/10.1021/acsami.4c12920.

44. A. Sundar, J. Park, H. Park, E. Lee, J. J. Kim, and P. Zapol, "Bayesian Optimization of Entropy-Stabilized Metal Fluoride Conversion Cathodes and Their Synthesis," *Journal of Power Sources* 635 (2025): 236448, https://doi.org/10.1016/j.jpowsour.2025.236448.

45. H. Wu, J. Hu, and C. Li, "Synergistic Effects of Carbon Dots and Heterojunctions to Enable Li–Fe–F All-Solid-State Ceramic Batteries With High Cathode Loading and Cumulative Capacity," *Materials Horizons* 12 (2025): 9837–9850, https://doi.org/10.1039/D5MH00727E.

46. Y. Bai, X. Zhou, Z. Jia, et al., "Understanding the Combined Effects of Microcrystal Growth and Band Gap Reduction for $Fe_{(1-x)}Ti_xF_3$ Nanocomposites as Cathode Materials for Lithium-Ion Batteries," *Nano Energy* 17 (2015): 140–151, https://doi.org/10.1016/j.nanoen.2015.08.006.

47. J. Li, S. Xu, S. Huang, L. Lu, L. Lan, and S. Li, "In Situ Synthesis of $Fe_{(1-x)}Co_xF_3$/MWCNT Nanocomposites With Excellent Electrochemical Performance for Lithium-Ion Batteries," *Journal of Materials Science* 53 (2018): 2697–2708, https://doi.org/10.1007/s10853-017-1685-2.

48. M. Liu, X. Wang, S. Wei, H. Hu, R. Zhang, and L. Liu, "Cr-Doped $Fe_2F_5H_2O$ With Open Framework Structure as a High Performance Cathode Material of Sodium-Ion Batteries," *Electrochimica Acta* 269 (2018): 479–489, https://doi.org/10.1016/j.electacta.2018.02.159.

49. C. Zhang, M. Yan, W. Li, et al., "Cr-Doped Fe_{1-x} Cr_xF_3 $0.33H_2O$ Nanomaterials as Cathode Materials for Sodium-Ion Batteries," *ACS Applied Materials & Interfaces* 13 (2021): 48653–48660, https://doi.org/10.1021/acsami.1c13462.

50. J. Ding, X. Zhou, H. Wang, J. Yang, Y. Gao, and J. Tang, "Mn-Doped $Fe_{1-x}Mn_xF_3{\cdot}0.33H_2O$/C Cathodes for Li-Ion Batteries: First-Principles Calculations and Experimental Study," *ACS Applied Materials & Interfaces* 11 (2019): 3852–3860, https://doi.org/10.1021/acsami.8b17069.

51. J. Ding, X. Zhou, C. Luo, et al., "First-Principles Calculations and Experimental Study of Al-Doped $Fe_{1-x}Al_xF_3{\cdot}0.33H_2O$/C Cathodes for Li-Ion Batteries," *Ionics* 28 (2022): 3127–3137, https://doi.org/10.1007/s11581-022-04503-9.

52. M. Liu, J. Liu, B. Chen, et al., "Unveiling the Role and Mechanism of Nb Doping and In Situ Carbon Coating on Improving Lithium-Ion Storage Characteristics of Rod-Like Morphology FeF_3 $0.33H_2O$," *Small* 18 (2022): 2105193, https://doi.org/10.1002/smll.202105193.

53. M. Liu, Q. Wang, B. Chen, et al., "Band-Gap Engineering of FeF_3 $0.33H_2O$ Nanosphere via Ni Doping as a High-Performance Lithium-Ion Battery Cathode," *ACS Sustainable Chemistry & Engineering* 8 (2020): 15651–15660, https://doi.org/10.1021/acssuschemeng.0c05258.

54. Y. Zhao, K. Wei, H. Wu, et al., "LiF Splitting Catalyzed by Dual Metal Nanodomains for an Efficient Fluoride Conversion Cathode," *ACS Nano* 13 (2019): 2490–2500.

55. F. Omenya, N. J. Zagarella, J. Rana, et al., "Intrinsic Challenges to the Electrochemical Reversibility of the High Energy Density Copper(II) Fluoride Cathode Material," *ACS Applied Energy Materials* 2 (2019): 5243–5253, https://doi.org/10.1021/acsaem.9b00938.

56. X. Hua, R. Robert, L. S. Du, et al., "Comprehensive Study of the CuF_2 Conversion Reaction Mechanism in a Lithium Ion Battery," *Journal of Physical Chemistry C* 2014, 118, 15169–15184.

57. W. Gu, A. Magasinski, B. Zdyrko, and G. Yushin, "Metal Fluorides Nanoconfined in Carbon Nanopores as Reversible High Capacity Cathodes for Li and Li-Ion Rechargeable Batteries: FeF_2 as an Example," *Advanced Energy Materials* 5 (2015): 1401148, https://doi.org/10.1002/aenm.201401148.

58. Y. Ma, S. Qing, H. Liu, et al., "Conversion-Type Cathode Materials for High Energy Density Solid-State Lithium Batteries," *Journal of Energy Chemistry* 100 (2025): 409–425, https://doi.org/10.1016/j.jechem.2024.09.001.

59. J. Casella, J. Morzy, F. C. Mocanu, et al., "Performance Comparison of Transition Metal (Cr, Mn, Fe, Co, Ni, Cu)-Fluoride Conversion Cathodes in Thin-Film Solid-State Batteries," *ACS Appl Energy Materials* 8 (2025): 15101–15111.

60. J. Sivavec, J. F. Baumgärtner, D. C. Stoian, et al., "On the Feasibility of Pairing Pyrochlore Iron(III) Hydroxy Fluoride Cathode With Argyrodite Li_6PS_5Cl Solid-State Electrolyte for Low-Cost All-Solid-State Batteries," *Batteries & Supercaps* 8 (2025): 202400731, https://doi.org/10.1002/batt.202400731.

61. K. L. Wilson, A. Halajko, F. Badway, B. Harrop, and G. G. Amatucci, "Iron Metal Based Positive Electrodes for Metal Fluoride High Energy Lithium Batteries," *Journal of The Electrochemical Society* 172 (2025): 010531, https://doi.org/10.1149/1945-7111/adacb3.

62. L. Xie, X. Zhang, H. Hu, et al., "Improved Interfacial Stability of an Iron Trifluoride Cathode With a Yolk–Shell Structure in Sulfide-Based All-Solid-State Lithium Batteries," *ACS Applied Materials & Interfaces* 17 (2025): 33036–33046, https://doi.org/10.1021/acsami.5c02940.

63. X. Zhou, M. Jiang, Y. Duan, et al., "Multi-Electron Transfer Halide Cathode Materials Based on Intercalation-Conversion Reaction Towards All-Solid-State Lithium Batteries," *Angewandte Chemie* 137 (2025): 202416635, https://doi.org/10.1002/ange.202416635.

64. L. Jia, J. Zhu, X. Zhang, B. Guo, Y. Du, and X. Zhuang, "Li–Solid Electrolyte Interfaces/Interphases in All-Solid-State Li Batteries," *Electrochemical Energy Reviews* 7 (2024): 12, https://doi.org/10.1007/s41918-024-00212-1.

65. W. Tang, R. Qi, J. Wu, et al., "Engineering, Understanding, and Optimizing Electrolyte/Anode Interfaces for All-Solid-State Sodium Batteries," *Electrochemical Energy Reviews* 7 (2024): 23, https://doi.org/10.1007/s41918-024-00228-7.

66. A. C. Luntz, J. Voss, and K. Reuter, "Interfacial Challenges in Solid-State Li Ion Batteries," *The Journal of Physical Chemistry Letters* 6 (2015): 4599–4604, https://doi.org/10.1021/acs.jpclett.5b02352.

67. Y. Liu, M. Lei, C. Lai, et al., "Enable High Reversibility of Fe/Cu Based Fluoride Conversion Batteries via Interfacial Gas Release and Detergency of Garnet Electrolytes," *Materials Today* 61 (2022): 65–77, https://doi.org/10.1016/j.mattod.2022.10.019.

68. J. Peng, X. Wang, H. Li, L. Chen, and F. Wu, "High-Capacity, Long-Life Iron Fluoride All-Solid-State Lithium Battery With Sulfide Solid Electrolyte," *Advanced Energy Materials* 13 (2023): 2300706, https://doi.org/10.1002/aenm.202300706.

69. B. Shao, S. Tan, Y. Huang, et al., "Enabling Conversion-Type Iron Fluoride Cathode by Halide-Based Solid Electrolyte," *Advanced Functional Materials* 32 (2022): 2206845, https://doi.org/10.1002/adfm.202206845.

70. G. Conforto, R. Ruess, D. Schröder, et al., "Editors' Choice—Quantification of the Impact of Chemo-Mechanical Degradation on the Performance and Cycling Stability of NCM-Based Cathodes in Solid-State Li-Ion Batteries," *Journal of The Electrochemical Society* 168 (2021): 070546, https://doi.org/10.1149/1945-7111/ac13d2.

71. W. Zhang, F. Richter, S. P. Culver, et al., "Degradation Mechanisms at the $Li_{10}GeP_2S_{12}/LiCoO_2$ Cathode Interface in an All-Solid-State Lithium-Ion Battery," *ACS Applied Materials Interfaces* 10 (2018): 22226–22236.

72. Y. Huang, B. Shao, and F. Han, "Interfacial Challenges in All-Solid-State Lithium Batteries," *Current Opinion in Electrochemistry* 33 (2022): 100933, https://doi.org/10.1016/j.coelec.2021.100933.

73. C. Yuan, H. B. Wu, Y. Xie, and X. W. Lou, "Mixed Transition-Metal Oxides: Design, Synthesis, and Energy-Related Applications," *Angewandte Chemie International Edition* 53 (2014): 1488–1504, https://doi.org/10.1002/anie.201303971.

74. T. Asano, A. Sakai, S. Ouchi, M. Sakaida, A. Miyazaki, and S. Hasegawa, "Solid Halide Electrolytes With High Lithium-Ion Conductivity for Application in 4 V Class Bulk-Type All-Solid-State Batteries," *Advanced Materials* 30 (2018): 1803075, https://doi.org/10.1002/adma.201803075.

Supporting Information

Additional supporting information can be found online in the Supporting Information section.

Supporting File: adfm75027-sup-0001-SuppMat.docx.